Stable lattice Boltzmann model for Maxwell equations in media

A. Hauser* and J. L. Verhey†

Department of Experimental Audiology, Otto von Guericke University Magdeburg, Leipziger Straße 44, 39120 Magdeburg, Germany

(Received 20 July 2017; revised manuscript received 3 November 2017; published 13 December 2017)

The present work shows a method for stable simulations via the lattice Boltzmann (LB) model for electromagnetic waves (EM) transiting homogeneous media. LB models for such media were already presented in the literature, but they suffer from numerical instability when the media transitions are sharp. We use one of these models in the limit of pure vacuum derived from Liu and Yan [Appl. Math. Model. **38**, 1710 (2014)] and apply an extension that treats the effects of polarization and magnetization separately. We show simulations of simple examples in which EM waves travel into media to quantify error scaling, stability, accuracy, and time scaling. For conductive media, we use the Strang splitting and check the simulations accuracy at the example of the skin effect. Like pure EM propagation, the error for the static limits, which are constructed with a current density added in a first-order scheme, can be less than 1%. The presented method is an easily implemented alternative for the stabilization of simulation for EM waves propagating in spatially complex structured media properties and arbitrary transitions.

DOI: 10.1103/PhysRevE.96.063306

I. INTRODUCTION

The lattice Boltzmann (LB) equation was originally developed for fluid simulations [1]. This algorithm, referred to as the lattice Boltzmann model (LBM) in the following, belongs to the lattice gas automaton describing a discretized microcanonical model of an incompressible fluid. The first applications on fluid simulations showed that the LBM was an efficient alternative to conventional numerical methods like those based on the finite difference time domain [2]. Later studies applied this approach to simulations of acoustics [3,4], non-Newton fluids [5], various interactions with boundaries [6–10] like reflection or pressure, multicomponent fluids [11], phase transitions [12], convection [13], and heat transport [14].

The LBM is used for simulations of a special type of ordinary differential equations (ODEs) including the limit of the equation of continuum in its parameter space. Different fields of physics with similarities in their ODEs compared to the equations underlying the LBM have been simulated, such as the Euler [15] or wave [16] equation, nonlinear and complex equations [17] like the nonrelativistic Schrödinger equation [18], or the one-dimensional relativistic Dirac equation [19] in quantum mechanics.

Dellar [20] first described the kinematics of ferrofluids via LBM and extended this model in following studies to simulations of magnetohydrodynamics [21]. Later studies considered other systems with properties that were described by the Maxwell equations [22,23]. For example, Liu and Yan [23] showed a LBM to improve the accuracy of the propagation of electromagnetic waves including the interaction with media. However, they showed only simulations in pure vacuum.

Mendoza and Muñoz [22] used a different approach for their LBM to simulate the propagation of electromagnetic (EM) waves into homogeneous media. They mentioned instabilities of simulations that could, according to the authors, be avoided by using smooth transitions between material properties.

The propagation of EM waves in inhomogeneous media has been shown by Hanasoge *et al.* [24] via the LB equation. The authors mentioned difficulties in numerical stability in the presence of sharp interfaces as well. They argue that these instabilities are the result of higher-order terms in the Chapman-Enskog expansion that may not be negligible anymore in such cases of high media gradients. It is known from other models that such instabilities are caused by the stiffness issue arising from varying magnitudes of properties in the time evolution schemes, such as multiphase flow [25,26]. In this paper, we derive a LBM of Ref. [23] for electromagnetism and suggest an extension that allows stable simulations of EM waves that propagate in a composition of homogeneous media modeled with arbitrary transitions including the limit of sharp interfaces.

Section II introduces the Maxwell equations and the evolution scheme of our LBM. The basic derivation of these equations and the underlying assumptions can be found in Appendix A. This LBM is analogous to the one described in Ref. [23] and is here called an "unseparated" model with the derivation of this model described in Appendix B. Then our model called "separated," an extension of the separated one in the limit of pure vacuum, is presented (see also Appendix C for more details as well). In Sec. III we show simulations of examples that are easy to comprehend. The boundary conditions of the first three examples are chosen to be periodic to ensure the total energy to be conserved over a large number of iteration steps. The first example analyzes the error of the total energy of an EM wave propagating from vacuum into a dielectric medium modeled with a sharp interface to show that our LBM is of second-order accuracy. The second example shows the evolution of total energy obtained from simulations with different methods (separation, smooth transition, entropic filter) suitable for stabilization as well as the unseparated model proposed in this work. The third example shows the amplitudes and velocities of the reflected and transmitted part of an EM wave packet before and after it passes a dielectric interface. We then show simulations with open boundary conditions of an EM wave penetrating a conductor. A broad range of conductivities for the limit of bad and good conductors

*Andreas.Hauser@med.ovgu.de
†Jesko.Verhey@med.ovgu.de

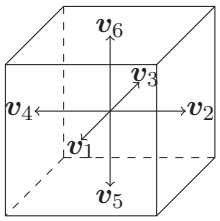

FIG. 1. A D3Q7 lattice and the directions of the velocity vectors $\boldsymbol{v}_i$ accompanying to their f_i within one cell.

is considered. Then the static limit of the electric field around a point charge and the magnetic field around a current each generated via a current density are shown. The properties of our approach are summarized and discussed in Sec. IV.

II. LATTICE BOLTZMANN MODEL

The LBM [27] is an approximation of the Boltzmann equation applied on a system that is divided into cells via a lattice. The discretized Boltzmann equation can be written as

$$f_i(\boldsymbol{r}+\boldsymbol{v}_i\delta t, t+\delta t) = f_i(\boldsymbol{r},t) + \sum_j \Omega_{ij}(\boldsymbol{r},t), \tag{1}$$

where f_i equals a particle density given at the time t and located in the cell denoted by the vector $\boldsymbol{r}$. This density is moving in direction $\boldsymbol{v}_i$ to its neighboring cell and takes with it a quantity defined by the collision matrix Ω_{ij}. Typically these cells are disposed into a grid that represent a lattice. We use a lattice known as "D3Q7" [28] where "D" denotes the dimension followed by its number and "Q" the number of lattice vectors followed by its number; such a lattice is shown in Fig. 1. A simple and commonly used case for Ω_{ij} is given by the Bhatnagar-Gross-Krook (BGK) collision operation with

$$\Omega_{ij}(\boldsymbol{r},t) = \frac{1}{\tau}\left[f_i^{\mathrm{eq}}(\boldsymbol{r},t) - f_i(\boldsymbol{r},t)\right], \tag{2}$$

where τ represents a relaxation time towards an equilibrium f_i^{eq}. The Chapman-Enskog expansion allows the prediction of the equation of continuum for $\tau = \frac{1}{2}$ [29] so that (1) reads

$$f_i(\boldsymbol{r}+\boldsymbol{v}_i\delta t, t+\delta t) = 2f_i^{\mathrm{eq}}(\boldsymbol{r},t) - f_i(\boldsymbol{r},t), \tag{3}$$

the so-called lattice BGK (LBGK) model. As a fixed value is assigned to τ, this model does not belong to the relaxation-type LBM in which τ represents properties of macroscopic transport mechanisms, like viscosity in fluid dynamics. Therefore this LBM works in a stream-and-compute local equilibria procedure. An expansion of (3) with $\tau = \frac{1}{2}$ up to the second order in δt approximates

$$\sum_i \left(\partial_t f_i^{\mathrm{eq}} + \sum_\alpha v_{\alpha_i}\partial_\alpha f_i^{\mathrm{eq}}\right) = 0, \tag{4}$$

where v_{α_i} represents the α component of $\boldsymbol{v}_i$ (see Appendix A for more details on the Chapman-Enskog expansion).

This equation of continuity is suitable for the simulation of electrodynamics via the Maxwell equations.

A. Maxwell equations

The Maxwell equations are a set of two linear homogeneous and two inhomogeneous differential equations

$$\sum_\alpha \partial_\alpha B_\alpha = 0, \sum_{\beta,\gamma}\epsilon_{\alpha\beta\gamma}\partial_\beta E_\gamma = -\partial_t B_\alpha,$$
$$\sum_\alpha \partial_\alpha D_\alpha = \rho, \sum_{\beta,\gamma}\epsilon_{\alpha\beta\gamma}\partial_\beta H_\gamma = \partial_t D_\alpha + j_\alpha, \tag{5}$$

with the Levi-Civita tensor $\epsilon_{\alpha\beta\gamma}$ in its standard definition, the vector components $\alpha,\beta,\gamma \in \{x,y,z\}$ of the magnetic induction $\boldsymbol{B}$, electric field $\boldsymbol{E}$, displacement field $\boldsymbol{D}$, charge density ρ, magnetic field $\boldsymbol{H}$, and the current density $\boldsymbol{j}$. The material equations are defined as

$$D_\alpha = \varepsilon_0 E_\alpha + P_\alpha \to \varepsilon_r\varepsilon_0 E_\alpha, \tag{6a}$$
$$B_\alpha = \mu_0(H_\alpha + M_\alpha) \to \mu_r\mu_0 H_\alpha, \tag{6b}$$

with the vacuum permittivity ε_0 (permeability μ_0), the relative permittivity ε_r (permeability μ_r), and the vectors of polarization $\boldsymbol{P}$ and magnetization $\boldsymbol{M}$. The arrow denotes the description for linear media. In the following, we set ε_0 and μ_0 to one and therefore the speed of light in vacuum defined by $\varepsilon_0\mu_0 = c^{-2}$ to one as well. As shown in Refs. [22,23], the focus laid on the use of $\nabla\times\boldsymbol{E} = -\dot{\boldsymbol{B}}$ and $\nabla\times\boldsymbol{H} = \boldsymbol{j} + \dot{\boldsymbol{D}}$ as one can derive from them

$$\partial_t \nabla\cdot\boldsymbol{B} = 0, \tag{7a}$$
$$\partial_t(\nabla\cdot\boldsymbol{D} - \rho) = 0 \tag{7b}$$

by using the conservation of charge density $D_t\rho = 0$. If they are valid for one time step, they are valid for all time steps, and all Maxwell equations are then fulfilled.

B. Macroscopic equations for propagation

According to Ref. [23], we use (A9) for the Maxwell equations in (5) for each vector component of $\boldsymbol{E}$ and $\boldsymbol{H}$. We introduce the distributions $e_{\alpha,i}(\boldsymbol{r},t)$, $h_{\alpha,i}(\boldsymbol{r},t)$ from which the macroscopic field components are computed:

$$\varepsilon_r E_\alpha(\boldsymbol{r},t) = \sum_i e_{\alpha,i}(\boldsymbol{r},t), \tag{8a}$$
$$\mu_r H_\alpha(\boldsymbol{r},t) = \sum_i h_{\alpha,i}(\boldsymbol{r},t). \tag{8b}$$

Using (3) for the time evolution of these distributions, we obtain

$$e_{\alpha,i}(\boldsymbol{r}+\boldsymbol{v}_i\delta t, t+\delta t) = 2e_{\alpha,i}^{\mathrm{eq}}(\boldsymbol{r},t) - e_{\alpha,i}(\boldsymbol{r},t), \tag{9a}$$
$$h_{\alpha,i}(\boldsymbol{r}+\boldsymbol{v}_i\delta t, t+\delta t) = 2h_{\alpha,i}^{\mathrm{eq}}(\boldsymbol{r},t) - h_{\alpha,i}(\boldsymbol{r},t) \tag{9b}$$

with their equilibria

$$e_{\alpha,i}^{\mathrm{eq}} = \frac{1}{6}\left(\varepsilon_r E_\alpha - \sum_{\beta,\gamma}\epsilon_{\alpha\beta\gamma}v_{\beta,i}H_\gamma\right), \tag{10a}$$
$$h_{\alpha,i}^{\mathrm{eq}} = \frac{1}{6}\left(\mu_r H_\alpha + \sum_{\beta,\gamma}\epsilon_{\alpha\beta\gamma}v_{\beta,i}E_\gamma\right). \tag{10b}$$

We refer to this LBM as an "unseparated" model because of ε_r and μ_r are part of the streaming step in (10). Now, using the equilibria (10) for the LB equations (9), we obtain the two Maxwell equations

$$\partial_t[\varepsilon_r E_\alpha(\boldsymbol{r},t)] = \sum_{\beta,\gamma} \epsilon_{\alpha\beta\gamma}\partial_\beta H_\gamma(\boldsymbol{r},t), \tag{11a}$$

$$\partial_t[\mu_r \partial_t H_\alpha(\boldsymbol{r},t)] = -\sum_{\beta,\gamma} \epsilon_{\alpha\beta\gamma}\partial_\beta E_\gamma(\boldsymbol{r},t) \tag{11b}$$

via the Chapman-Enskog expansion as derived in Appendix B.

The propagation of an EM wave simulated with this LBM remains stable in homogeneous media without transitions. We chose the vacuum limit with $\varepsilon_r = 1$ and $\mu_r = 1$ (vacuum) for (10) and take additional distributions $e^{\mathrm{eq}}_{\alpha,0}$ and $h^{\mathrm{eq}}_{\alpha,0}$ that belong to the zero vector in order to "separate" the interaction with media. We do this by defining $e^{\mathrm{eq}}_{\alpha,0} = P_\alpha := (\varepsilon_r - 1)E_\alpha$ and $h^{\mathrm{eq}}_{\alpha,0} = M_\alpha := (\mu_r - 1)H_\alpha$ so that the equilibria of that separated model are

$$e^{\mathrm{eq}}_{\alpha,i} = \begin{cases} \frac{1}{6}\left(E_\alpha - \sum_{\beta,\gamma}\epsilon_{\alpha\beta\gamma}v_{\beta,i}H_\gamma\right) & \text{if } i \neq 0 \\ (\varepsilon_r - 1)E_\alpha & \text{if } i = 0 \end{cases}, \tag{12a}$$

$$h^{\mathrm{eq}}_{\alpha,i} = \begin{cases} \frac{1}{6}\left(H_\alpha + \sum_{\beta,\gamma}\epsilon_{\alpha\beta\gamma}v_{\beta,i}E_\gamma\right) & \text{if } i \neq 0 \\ (\mu_r - 1)H_\alpha & \text{if } i = 0. \end{cases} \tag{12b}$$

With these equilibria, we obtain the same Maxwell equations (11) as shown in Appendix C. Both share the same scaling properties like the iteration time step $\delta t = \frac{1}{6}$ and the speed of light in lattice units $\tilde{c}_0 := \Delta N_{\mathrm{cell}}/\Delta N_{\mathrm{it}} = \frac{1}{3}$ with the number of lattice cell N_{cell} and iteration step N_{it}.

C. Extension to conductive media and currents

Adding the current density $\boldsymbol{j}$ as a source to the model is done by using the Maxwell-Ampère law $\varepsilon_r\mathbf{E} + \mathbf{j} = \nabla \times \mathbf{H}$. Here we take the commonly used first-order scheme [23,30] approximation by updating

$$E_\alpha \rightarrow E_\alpha + \delta t j_\alpha \tag{13}$$

after each iteration step. This approach is suitable for external sources. Conductive media, described by

$$\mathbf{j} = \sigma\mathbf{E} \tag{14}$$

with σ as scalar conductivity, can be treated in the same way if σ is close to zero. Simulations with $\sigma \gg 0$ are less accurate, and the simulation gets rapidly unstable. In order to avoid this instability, we use the sequential Strang splitting [31] via

$$\varepsilon_r\partial_t\nabla\cdot\mathbf{E} = -\sigma\nabla\cdot\mathbf{E} \tag{15}$$

with the solution

$$\nabla\cdot\mathbf{E}(t+\delta t) = \nabla\cdot\mathbf{E}(t)e^{-\sigma/\varepsilon_r\delta t}. \tag{16}$$

We then make use of $\mathbf{E}(t+\delta t) = \mathbf{E}(t)e^{-\sigma/\varepsilon_r\delta t}$, which holds

$$\varepsilon_r\dot{\mathbf{E}}(t+\delta t) + \sigma\mathbf{E}(t+\delta t) = \varepsilon_r\dot{\mathbf{E}}(t)e^{-\sigma/\varepsilon_r\delta t}. \tag{17}$$

After each iteration, we replace $\mathbf{E} \rightarrow \mathbf{E}e^{-\sigma/\varepsilon_r\delta t}$ and use this new field in combination with $\varepsilon_r\dot{\mathbf{E}} = \nabla\times\mathbf{H}$ for the next iteration so that it depends on $t + \delta t$:

$$\begin{aligned}\nabla\times\mathbf{H}(t) &= \varepsilon_r\dot{\mathbf{E}}(t)e^{-\sigma/\varepsilon_r\delta t} \\ &\approx \varepsilon_r\dot{\mathbf{E}}(t) + \sigma\mathbf{E}(t).\end{aligned} \tag{18}$$

Considering $\nabla\times\mathbf{E} = -\mu_r\dot{\boldsymbol{H}}$, we assume that only the spatial distribution of $\boldsymbol{E}$ leads to temporal change of $\boldsymbol{H}$ since $\nabla\times(\boldsymbol{E}e^{-\sigma/\varepsilon_r\delta t}) \equiv \nabla\times\boldsymbol{E}$. This approximation works well in the case for small values of σ. As mentioned earlier, the agreement between theoretical prediction and simulation under high conductivities can be less accurate, but as shown later the simulation remains stable even under unphysically high σ.

III. SIMULATION RESULTS

A. Error scaling

We now simulate the propagation of an EM wave in a one-dimensional system with periodic boundaries to obtain the error scaling of the presented LBM. The initial value for the EM fields is zero except for

$$E_y(x, N_{\mathrm{it}} = 0) \equiv H_z(x, N_{\mathrm{it}} = 0) := e^{-250(\frac{x}{N_x} - \frac{1}{4})^2}, \tag{19}$$

in a lattice with a specific size defined by the number of cells N_x that are used. The media parameters of the system are defined with $\sigma(x) = 0$, $\mu_r(x) = 1$ and

$$\varepsilon_r(x) = \begin{cases} 1 & \text{if } x < \frac{N_x}{2} \\ 10 & \text{if } x \geqslant \frac{N_x}{2} \end{cases} \tag{20}$$

for $x \in [0, N_x]$. In order to compare the unseparated model described by (10) with the separated one described by (12), we calculate the total energy, which reads

$$W := \frac{1}{2}\sum_{x=0}^{N_x}[\varepsilon_r(x)\boldsymbol{E}^2(x) + \mu_r(x)\boldsymbol{H}^2(x)] \tag{21}$$

and compare the simulation results with the theoretical prediction W_{th} by calculating the error

$$\Delta W(N_{\mathrm{it}}) := |W(N_{\mathrm{it}}) - W_{th}| \tag{22}$$

at each iteration step.

Figure 2 shows the time evolution of ΔW of the separated and unseparated model. The size of the system defined by (20) was chosen with $N_x = 100$. Both simulations started with equal errors as the wave packet defined with (19) was almost only in vacuum. At $N_{\mathrm{it}} = 400$, the major part of the initialized wave packet propagated into the dielectric. The error of the unseparated model remains nearly unchanged at the first $N_{\mathrm{it}} = 4000$ iteration steps but then tends to infinity very quickly. In contrast, the error of the separated model starts to rise already at the iteration step $N_{\mathrm{it}} = 400$ but remains at the relative error of about 10^{-4}.

As we have used the linear ODE defined (A9), we expect our LBM to remain of second-order accuracy in form of

$$\Delta W \propto (\delta x)^2 \tag{23}$$

with the spatial steps δx. Decreasing δx can be achieved by increasing the number of grid cells with N_x. The initial condition defined by (19) allows the relation $N_x \propto \delta x^{-1}$. Figure 3 shows the relation $\Delta W \propto \delta x^{1.98}$, which confirms

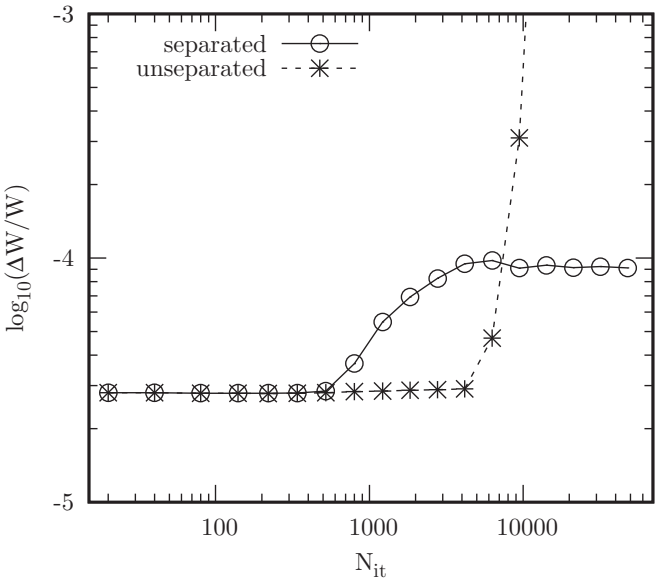

FIG. 2. Error of total energy ΔW at iteration step N_{it} of the model derived from Ref. [23] (unseparated) and our model (separated) of an EM wave propagating into a dielectric medium. Both simulations were defined via (19) and (20) and $N_x = 100$.

the expected second-order convergence of (23). Here we repeated the simulation paradigm that was used for the simulations shown in Fig. 2 for various N_x. The monitored error then was averaged over the iteration period of $N_{\text{it}} \in [0, 10^4]$.

B. Numerical stability

For the investigation of numerical stability, we check if our LBM is able to fulfill the conservation of energy. We therefore chose a two-dimensional 200×200 lattice with periodic boundary conditions in each direction. The third dimension here is therefore represented via an infinite alignment of this

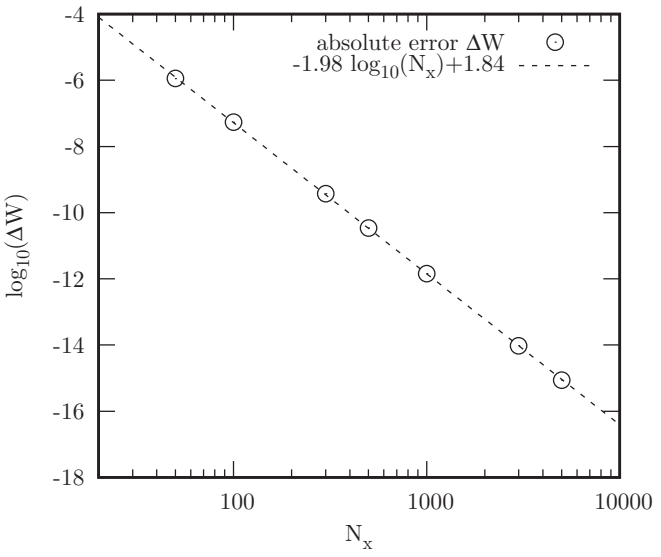

FIG. 3. Average absolute error ΔW at different lattice sizes defined by N_{it} and its regression curve. The error is obtained by averaging ΔW over 10^4 iterations for each lattice size.

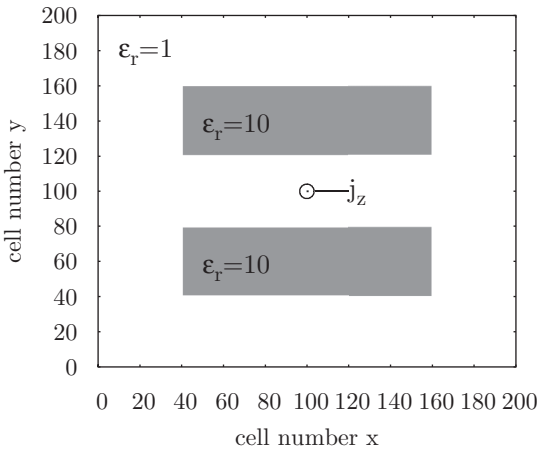

FIG. 4. 200×200 lattice with dielectric media $\varepsilon_r = 10$ (gray area) in vacuum. EM fields are generated by the current density j_z represented by the encircled black dot in the middle of the system (100,100).

two-dimensional plane in which the EM fields are fueled by the current density

$$j_z = \sin\left(N_{\text{it}} \frac{\pi}{50}\right) \tag{24}$$

radiating over the first 50 iterations. Figure 4 shows the setup of the material properties with $\varepsilon_r = 10$ in the gray area, $\varepsilon_r = 1$ elsewhere, and $\mu_r = 1$ and $\sigma = 0$ globally. The current density in the middle of the system is represented by the little encircled black dot. After the first 50 iterations, we expect the total energy, calculated analogously to (21), to be constant in time. Here the results of three approaches suitable for stabilization are shown in Fig. 5. The first one (empty circles) is the separated LBM, which is compared with the unseparated one (filled circles). The second method (triangles) is the smoothed transition approach, as proposed in Refs. [22,24]. Here we used a linear change of material properties to represent the sharp interface between vacuum and medium. The third one (diamonds) is the entropic filtering as described in Refs. [32,33]. Here two different values for the relaxation time τ were used. The damping of the entropic filter with $\tau = 1.95^{-1}$ is too strong, since it causes the energy to rapidly decrease in time. For $\tau = 1.99^{-1}$, the energy first drops slightly too, to $N_{\text{it}} = 400$, but increases after that time overexponentially. Better results can be achieved by using a smooth transition. Here we compared the effects of five and 50 cells to smooth the sharp transition. As expected, the energy is conserved far longer using 50 cells than five or no cells (black squares of Fig. 5) for the transition.

Figure 6 shows the distribution of the energy density between unseparated (left column) and the separated model (right column) at different iteration steps. As shown in Fig. 5, the energy of the unseparated model (black filled squares) starts to increase significantly at about $N_{\text{it}} = 300$. This increase is visible in Fig. 6 as noise at the edges of the dielectrica and in the space between them. This noise keeps expanding between these media (see $N_{\text{it}} = 400$) and spreads all over the whole system as one can see at $N_{\text{it}} = 500$. In contrast, the separated

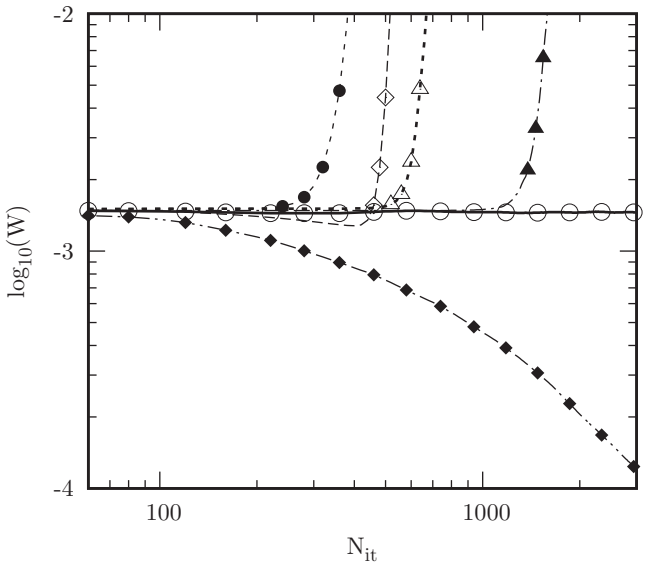

FIG. 5. Comparison of different techniques to stabilize the total energy W of an EM wave generated by an electric current $j_z = \sin(\pi N_{\rm it}/50)$ radiating in the middle of the system the first 50 iterations. The system is defined with periodic boundary conditions as shown in Fig. 4. The simulation with sharp media transition using the unseparated model is compared to the separated one, the smoothed transition, and the entropic filtering method.

model with splitting remains stable with a reasonable energy distribution.

C. Propagation of an electromagnetic wave

A well-known influence of media on the propagation of EM waves is the reduction of velocity. First, we compare simulation results of the separated model with the unseparated one (derived from Ref. [23]). The top left panel of Fig. 7 shows a Gaussian-shaped EM pulse that was initialized in vacuum (left white area). This pulse then is moving into a dielectric medium with $\varepsilon' = 9$ (right gray area). The amplitudes of H_y and E_z for the initial EM pulse were set to one. On a short time scale ($N_{\rm it} = 1000$) no significant differences were observed between the two models. Thus, only the simulations of the separated model are shown (top left panel of Fig. 7). The transmitted maximum has an average amplitude of 0.4992 and the reflected one has 0.5001. The analytical solution for the transmitted $E_{z,T}$ and reflected $E_{z,R}$ amplitude of the EM wave are given by [34]

$$\frac{E_{z,T}}{E_{z,0}} = \frac{2}{\sqrt{\frac{\varepsilon'}{\varepsilon}} + 1}, \tag{25a}$$

$$\frac{E_{z,R}}{E_{z,0}} = 1 - \frac{E_{z,T}}{E_{z,0}}, \tag{25b}$$

from which we obtain an amplitude for the transmitted and reflected electric field of 0.5, i.e., the simulations deviate from the theoretical values by less than 1%. The panels below the top one of Fig. 7 show snapshots at different time steps of the separated (left) and the unseparated model (right). The right one shows an increasingly unstable behavior with unexpected

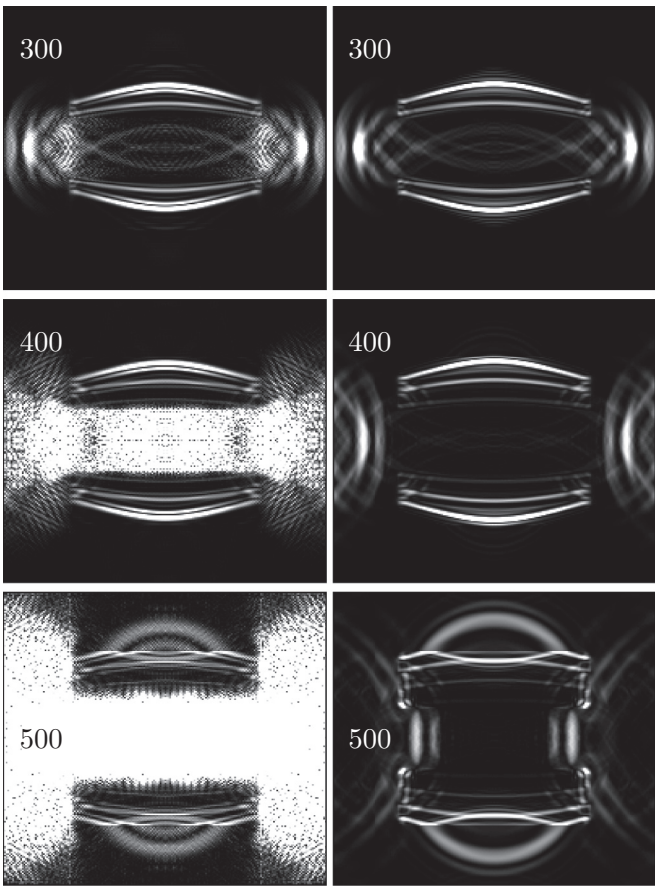

FIG. 6. Snapshots of distributed energy density of the electromagnetic wave simulations with unseparated (left column) and separated (right column) model at different iteration steps $N_{\rm it}$ The fields are generated with a current that is placed in the middle of the 200×200 cells system in which the EM waves cross dielectric media (not visible here; see Fig. 4).

oscillations, especially in vacuum (best seen in the bottom right panel for $N_{\rm it} = 7000$) that seems to be radiated from the surface of the medium into the vacuum. Similar to Fig. 6, these oscillations grow rapidly in the vacuum region near the media but not inside the medium. The inside of the media remains at that point nearly stable but on a longer time scale the oscillations occur in here as well (not shown). Now, the velocity of the EM pulse that travels from the beginning of the simulation to the moment it crosses the dielectric interface is determined. Figure 8 shows the position of the extrema of the amplitudes of the electric field over the time for the separated model. Until the iteration step $N_{\rm it} = 600$, the pulse propagates in vacuum only. From the relation between spatial position and time, the speed of light in vacuum can be obtained via linear regression as $\tilde{c}_0 = 0.3333 \pm 0.08\%$ (tilde denotes lattice units). For the reflected part at $N_{\rm it} > 600$, we obtain $\tilde{c}_r = 0.3303 \pm 0.25\%$. These predictions are in good agreement with the theoretical values of $\tilde{c}_0 \equiv \tilde{c}_r = 0.\overline{3}$. Inside the medium, the velocity of the transmitted wave was determined to be $\tilde{c}_t = 0.1114 \pm 0.18\%$ which is in good agreement with the theoretical value of $\tilde{c}_t = 0.\overline{1}$. Here we have shown the effects of media on the speed of light with permittivity $\varepsilon_r > 1$ only, but the expectations with inclusion

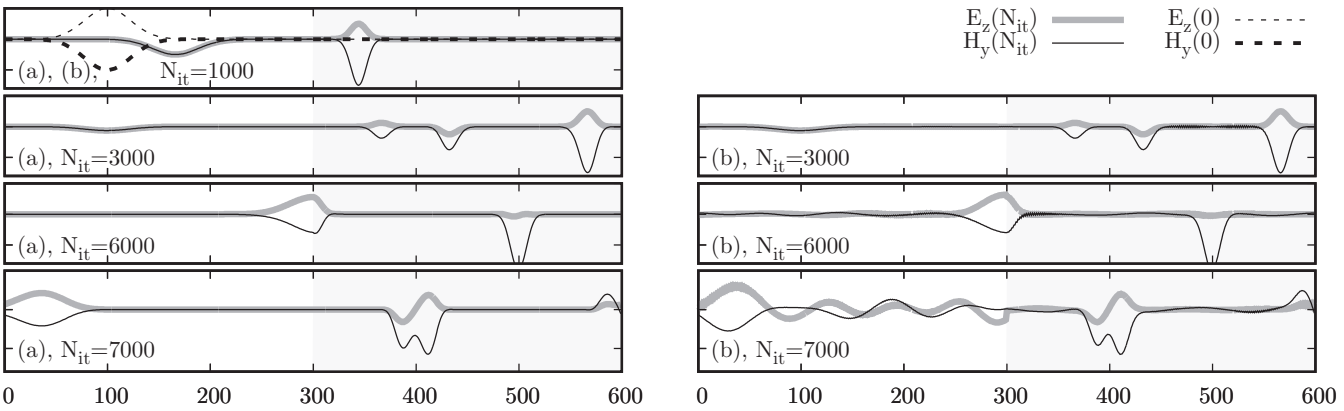

FIG. 7. Comparison between simulations on the basis of Eq. (12) (a, left column) with those based on Eq. (10) (b, right column). An one-dimensional Gaussian-shaped EM pulse travels through a 600-cells-wide lattice with periodic boundaries initialized in vacuum ($\varepsilon = 1$) and crossing a dielectric ($\varepsilon' = 9$, transparent gray area) interface starting at cell number 300 and ending at 600. Simulations at $N_{\mathrm{it}} = 0$ and at $N_{\mathrm{it}} = 1000$ are almost identical between these two approaches. At $N_{\mathrm{it}} = 3000$, one observes in (a) the first results of inaccuracies in the area of cells 200 to 300 (outside dielectric) and inside noised curves around cell 500. This unphysical behavior grows in strength over time as one can see at $N_{\mathrm{it}} = 6000$ and clearly at $N_{\mathrm{it}} = 7000$ as these inaccuracies tend to grow exponentially with iteration step.

of permeability $\mu_r > 1$ are of comparable accuracy (not shown here).

D. Skin effect

For an EM wave propagation inside a conductor, we chose the well-known predictions of the skin effect to compare the simulation results with. Therefore, we set the fields outside the conductor at a fixed position to

$$\boldsymbol{E} = E_0 \sin(\omega t)\boldsymbol{e}_y, \tag{26a}$$

$$\boldsymbol{H} = H_0 \sin(\omega t)\boldsymbol{e}_z, \tag{26b}$$

with $t = \frac{1}{3}N_{\mathrm{it}}$ and let the wave propagate in the x direction. With a typical complex ansatz for the dependency of E_y and H_z from t and x with $\exp[i(\omega t - kx)]$, one obtains the complex solution for the wave vector

$$k = \frac{\omega}{c}\left[1 + \left(\frac{\sigma}{\omega\varepsilon}\right)^2\right]^{1/4} \exp\left[-\frac{i}{2}\arctan\left(\frac{\sigma}{\omega\varepsilon}\right)\right] \tag{27}$$

that leads to a phase shift and weakened amplitudes from which one obtains

$$E_y(x) = E_0 \exp[-\Im(k)x] \sin[\omega t - \Re(k)x], \tag{28a}$$

$$H_z(x) = H_0 \exp[-\Im(k)x] \sin[\omega t - \Re(k)x + \Delta\phi], \tag{28b}$$

$$\Delta\phi = \frac{1}{2}\arctan\left(\frac{\sigma}{\omega\varepsilon}\right) = \Re(k)\Delta\lambda \tag{28c}$$

with the depth from the surface of the conductor x, the skin depth $d := \Im(k)$, the phase shift between E_y and H_z with $\Delta\phi$, and the resulting shift of wavelength $\Delta\lambda$. The impedance obeys

$$|Z| =: \frac{E_0}{H_0} = c\mu\left[1 + \left(\frac{\sigma}{\omega\varepsilon}\right)^2\right]^{-1/4}. \tag{29}$$

With an increased value of σ, the real part of (27) predicts a shortened wavelength

$$\lambda = \frac{2\pi}{\Re(k)}, \tag{30}$$

and the reduced speed of propagation c_σ inside the conductor follows

$$c_\sigma = \frac{\left[1 + \left(\frac{\sigma}{\omega\varepsilon}\right)\right]^{-1/4}}{\cos\left[\frac{1}{2}\arctan\left(\frac{\sigma}{\omega\varepsilon}\right)\right]} c_0. \tag{31}$$

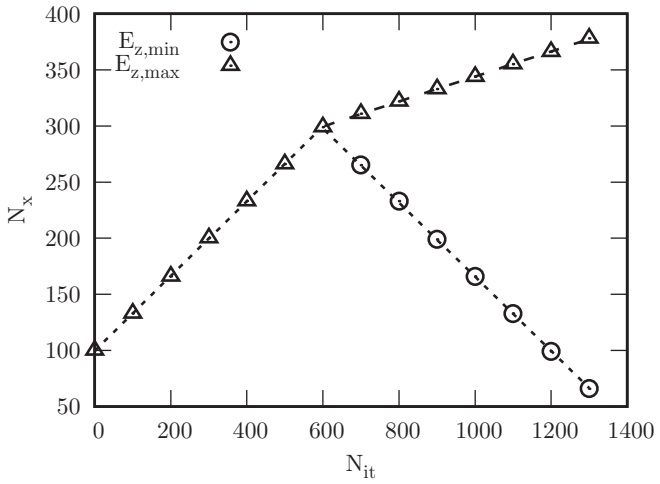

FIG. 8. According to case (a) of Fig. 7, the position of the maximum and minimum of E_z in time is shown. Here $E_{z,\min}$ corresponds to the reflected part of the EM wave. $E_{z,\max}$ of $N_{\mathrm{it}} < 600$ belongs the initial EM wave and the transmitted one to $N_{\mathrm{it}} \geqslant 600$.

Figure 9 compares the theoretical predictions of various quantities with data and extrema (minimum and maximum via error bars) obtained from simulations depending on the conductivity in a one-dimensional system consisting of 1000 cells. We have chosen $\omega = 2\pi/1000$, the initial amplitudes (26) equal to one (outside the conductor) and $\sigma = 10^n$ with $n \in [-5,1]$ to cover a broad range of conductivities including the limits of bad $\sigma \ll \omega\varepsilon$ and good $\sigma \gg \omega\varepsilon$ conductors (see $n \approx 3$ as a transition point). With $c_{\sigma=10}$ reduced down to 3.54%

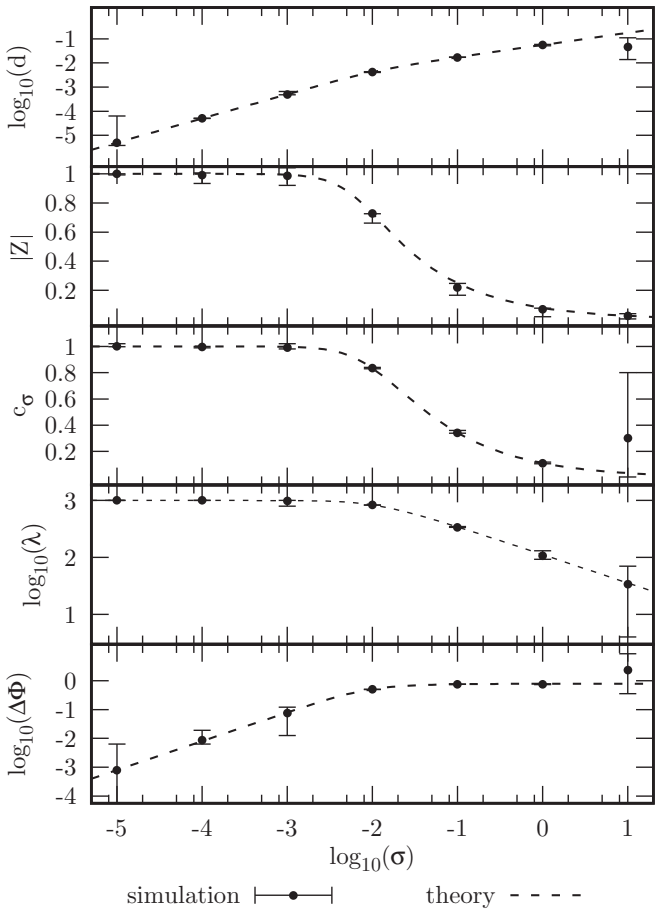

FIG. 9. An EM wave with $\omega = \frac{2\pi}{1000}$ penetrating a conductor. Theoretical prediction of the skin depth d, impedance $|Z|$, speed of propagation c_σ, wavelength λ, and phase shift $\Delta\phi$ depending on the conductivity σ are compared with simulation results. The error bars refer to the minimum and maximum that were obtained during the monitoring.

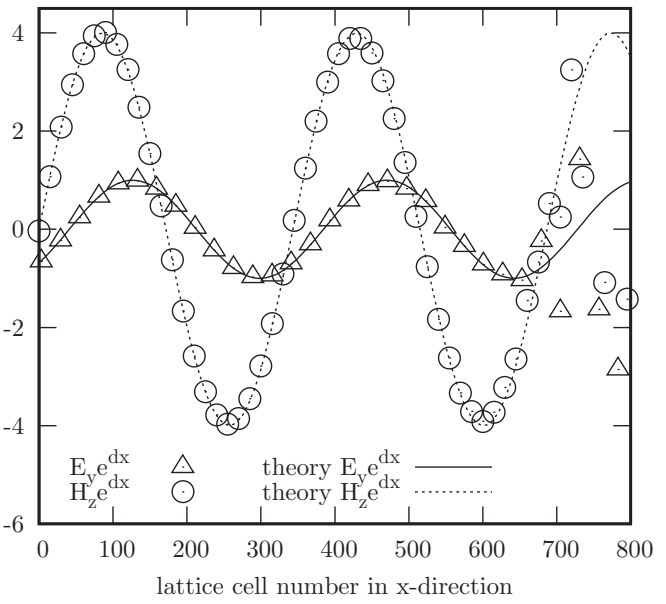

FIG. 10. The amplitudes of an EM wave (initialized with $\omega = 2\pi/1000$, $E_y = 1$, $H_z = 1$) propagating in a (good) conductor with $\sigma = 0.1$ in the x direction is compared with the theoretical prediction. The amplitudes E_y and H_z are amplified by $\exp(dx)$ with $d = 0.017176716$, the real part of (27). The numerical noise being amplified is visible at $x = 650$ and dominating the further curve.

of c_0, the waves need approximately 10^4 iterations to travel through the system. We therefore considered only data after $N = 10^6$ iterations (100 waves traveling through the system) as we expect that the waves then are nearly infinitely expanded. Monitoring the maxima and zeros of E_y and H_z over time, we have chosen the biggest values at each position in time. From these data, we determined values for the skin depth d via the logarithm of the maxima, $|Z|$ via their ratios, c_σ the zero of E_y over time, λ via differences of zeros of E_y and $\Delta\phi$ via differences of zeros between H_z and E_y. All these quantities fit well with the prediction except for $\sigma = 10$, here especially for c_σ and $\Delta\phi$. Because of $\lambda/2$ being theoretically 17.7 cells broad, the obtained data from simulation got more inaccurate since we searched for cells with E_y most closely to zero only. Similar to these inaccuracies, the rather big error bar of $\Delta\phi$ for $\sigma = 10^{-5}$ is caused by the finite error of $\Delta\lambda = 1$.

Good conductors, as shown in Fig. 10, are in good agreement with the prediction. Here a snapshot of the simulation already discussed in the context of Fig. 9 for $\sigma = 0.1$ is shown. As the strong weakening leads to a rapid drop of the amplitudes with the penetration depth, we amplified the data with the theoretical term $\exp(0.017176716\,x)$ to compensate for this attenuation. The phase shift between E_y and H_z is visible up to the penetration depth of about $x = 650$, as well as their wavelengths and their different amplitudes that are caused by the impedance. At that depth, the theoretical amplitudes are smaller (about 10^{-5} compared to the initial amplitude of one) than the numerical noise, which has an approximately constant amplitude at each point of the system.

E. Static limits

As the present model explicitly allows the derivation of Maxwell equations that only describe the propagation with (11), we now want to check if it implicitly contains the static limit in the form of (7) too. The two-dimensional system considered here contains 600×600 cells with open boundary conditions in the x-y plane. Figure 11 shows the curve of the field components H_y and E_x in the x direction.

For the magnetostatic case, a current in the z direction flows perpendicular towards the plane of the lattice with periodic boundary conditions in the z direction. Using the finite Stokes integral to calculate the results using 60 different circumferences, we obtained $\mathbf{j}_z = 0.999969 \pm 0.00113\%$. The electrostatic case is constructed by setting a current j_x from the center to the border of the lattice in the x direction. Only for the first 100 iterations, the current is set to 0.1; elsewhere it is $j_x = 0$. It then accumulates a charge with a theoretical value of $q = j_x \Delta T = j_x \frac{1}{3} \Delta N_{\text{it}} = \frac{10}{3}$. With the use of the finite Gauß integral over 60 different surfaces, we obtained $q = 3.33438 \pm 0.1221\%$. Both cases agree well with the theoretical values derived from (7).

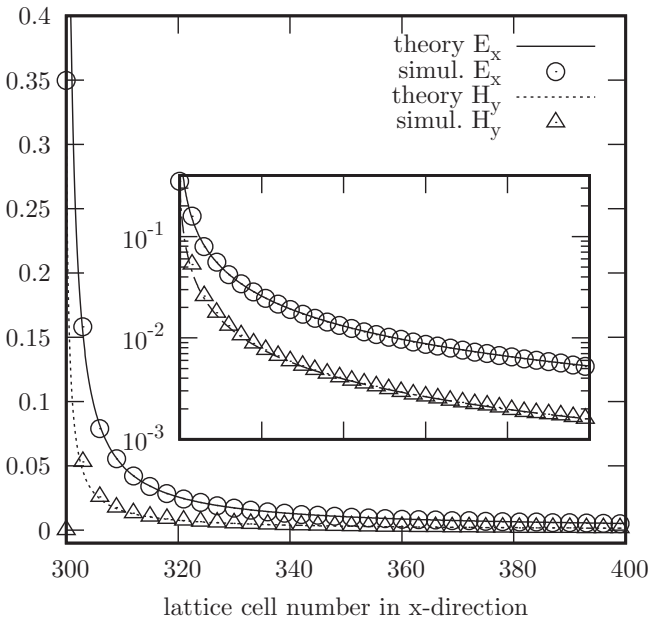

FIG. 11. Comparison of the simulated electrostatic field component E_x of a point charge and the magnetostatic field component H_y of an electrical current with the theoretical prediction.

IV. DISCUSSIONS AND CONCLUSIONS

The LBGK model based on Refs. [20,21,23] shows an efficient and simple way to simulate Maxwellian electrodynamics. Simulations of EM waves propagating into homogeneous media, however, are highly unstable, as shown in Fig. 2. Here the curve labeled "unseparated" shows the overexponential growth of the relative error of total energy in time. It is well known that LBGK, in general, tends to instabilities in certain limits of its applications [32,33,35–38]. The commonly used approaches to stabilize LBMs are the so-called semi- or fully implicit approximations for the Boltzmann equation [39] that, in general, need additional computation locally [40] on their distributions f_i. Such an implicit scheme for the EM propagation was used by Dellar [20] for only vacuum-like conductors. His model, in which the relaxation time is related to the conductivity, is not suitable for nonconductive media. In that case, the relaxation time, which is reversely related to the conductivity, tends to infinity in the limit of nonconductive media. At that point, the contribution from the collision term in the streaming step vanishes and the simulation returns unreasonable results. However, even if implicit schemes are able to reduce the second-order truncation error, it is questionable if this reduction is sufficient enough to avoid the mentioned instabilities caused by the description of media in (10). Another possibility for stabilizing of simulations with media transitions is to smooth interfaces between different media [22,24]. Such blurring of structures is impractical, since one has to increase the lattice size to ensure a reasonable resolution of the structure. This increases the required computation time and calculation memory. The authors suggested another possibility for stabilization by using a form of Boltzmann's H theorem [35]. However, for the H theorem, a nontrivial real root of a nonlinear system of equations has to be found. Such solutions (oftentimes being complex) are not always guaranteed. In addition, finding this root also increases calculation time substantially, which limits its use in practical aspects.

Another promising method is the "entropy trimming" [32,33,41,42] or filtering. Here the nonequilibrium entropy is reduced via an increased relaxation time at lattice points, in which the nonequilibrium entropy exceeded a predefined critical value. The disadvantage is that this violates (A9), and the second-order contributions then play a physical role like the viscous stress tensor in fluid dynamics. However, as the present LBM has to avoid these higher-order contributions, simulations will inevitably be not of second-order accuracy. One might consider a multi-relaxation time-based model for each field $\boldsymbol{E}$ and $\boldsymbol{H}$ as well. But as those parts of the Maxwell equations that describe the propagation in media are a set of linear differential equations, the use of a model suited for nonlinear convection diffusion [43] would need a proper, quite more complex or different collision model than the LBGK. The development of such a model is not the aim of the present work.

We have shown an easy extension of a special limit (vacuum) via additional and adapted LB equations that contain media properties described by polarization and magnetization. The presented model leads to stable simulation results under arbitrary media transitions. We achieve the same results by choosing the equilibria of these new distributions only with spatial derivation for their underlying equation of continuity, which therefore forces the partial time derivation to be zero. Note the influence of the dimension on stability. The unseparated model in Fig. 6 (two-dimensional), e.g., gets unstable at $N_{\mathrm{it}} = 300$, which is far earlier than in Fig. 7 (one-dimensional) with $N_{\mathrm{it}} = 6000$. In contrast to the unseparated model, we did not find any hint that our separated model gets unstable on larger iteration numbers in a three-dimensional system. The description of conductive media in our study is done via an extension of the elaborated model for propagation (12). Here we used a sequential first-order Strang splitting. The main advantage of this effective damping is to guarantee numerical stability. The applied simulations for the skin effect have shown to be accurate over a broad range of conductivities. As expected, the limit of good conductors suffers of accuracy. Here a combination with Ref. [20] could lead to better results via the extension to homogeneous media. For inhomogeneous media, one might consider [24] to be used for simulations including nonconductive media. Overall, the presented extension of the LBM for electrodynamics allows now a reliable, stable, and therefore practical tool for long-time simulations with arbitrary media transitions.

ACKNOWLEDGMENTS

We wish to thank Johannes Richter for his fruitful suggestions and corrections of a previous version of this manuscript.

APPENDIX A: CHAPMAN-ENSKOG EXPANSION

The Chapman-Enskog expansion is a method to derive the differential equation that describes the evolution of a quantity f being described by the Boltzmann equation. We chose the

BGK model (2) for the Boltzmann equation (1) and obtain

$$f_i(\boldsymbol{r}+\boldsymbol{v}_i\delta t,t+\delta t)=f_i(\boldsymbol{r},t)+\frac{1}{\tau}\left[f_i^{\mathrm{eq}}(\boldsymbol{r},t)-f_i(\boldsymbol{r},t)\right]. \tag{A1}$$

A Taylor series expansion is now applied to the left-hand side of (A1) that then reads

$$\begin{aligned} f_i(\boldsymbol{r}+\boldsymbol{v}_i\delta t,t+\delta t)=&f_i(\boldsymbol{r},t)+\delta t\,D_i f_i(\boldsymbol{r},t)\\ &+\frac{\delta t^2}{2}D_i^2 f_i(\boldsymbol{r},t)+O(\delta t^3) \end{aligned} \tag{A2}$$

with the temporal step δt and the total temporal derivation

$$D_i:=\partial_t+\sum_{\alpha\in\{x,y,z\}}v_{\alpha,i}\partial_\alpha. \tag{A3}$$

The Chapman-Enskog expansion now makes the ansatz that f_i and D_i each are expressed as a power series of δt that reads

$$f_i:=\sum_{n=0}\delta t^n f_i^{(n)}, \tag{A4a}$$

$$D_i:=\sum_{n=0}\delta t^n D_i^{(n)}. \tag{A4b}$$

We then use Eqs. (A4) and (A2) and insert them into (A1). Under the assumption $D_i\approx D_i^{(0)}$, we sort terms with same potency of δt up to the second order and get the following equations:

$$\delta_t^0:\quad f_i^{(0)}=f_i^{\mathrm{eq}}, \tag{A5a}$$

$$\delta_t^1:\quad f_i^{(1)}=-\tau D_i^{(0)}f_i^{(0)}, \tag{A5b}$$

$$\begin{aligned} \delta_t^2:\quad f_i^{(2)}&=-\tau\left(D_i^{(0)}f_i^{(1)}+\frac{1}{2}D_i^{(0)2}f_i^{(0)}+D_i^{(1)}f_i^{(0)}\right)\\ &=\left(\tau^2-\frac{\tau}{2}\right)D_i^{(0)2}f_i^{(0)}-\tau D_i^{(1)}f_i^{(0)}. \end{aligned} \tag{A5c}$$

With these expressions for $f_i^{(n)}$, we get for (A4a)

$$f_i=f_i^{\mathrm{eq}}-\tau D_i f_i^{\mathrm{eq}}\delta t+\left(\tau^2-\frac{\tau}{2}\right)D_i^2 f_i^{\mathrm{eq}}\delta t^2+O(\delta t^3). \tag{A6}$$

Under the assumption of $\sum_i f_i=\sum_i f_i^{\mathrm{eq}}$, we obtain with (A6)

$$\begin{aligned} \sum_i f_i^{\mathrm{eq}}=\sum_i\Big[&f_i^{\mathrm{eq}}-\tau D_i f_i^{\mathrm{eq}}\delta t\\ &+\left(\tau^2-\frac{\tau}{2}\right)D_i^2 f_i^{\mathrm{eq}}\delta t^2+O(\delta t^3)\Big] \end{aligned} \tag{A7}$$

from which we derive

$$D_i\sum_i f_i^{\mathrm{eq}}\approx\delta t\left(\tau-\frac{1}{2}\right)D_i^2\sum_i f_i^{\mathrm{eq}}. \tag{A8}$$

Using $\tau=\frac{1}{2}$ and (A3) for (A8), we obtain

$$\sum_i\left(\partial_t f_i^{\mathrm{eq}}+\sum_\alpha v_{\alpha_i}\partial_\alpha f_i^{\mathrm{eq}}\right)\approx 0, \tag{A9}$$

which approximates the equation of continuity for the quantity $\sum_i f_i^{\mathrm{eq}}$ with second-order accuracy.

APPENDIX B: UNSEPARATED MODEL

Deriving the macroscopic field components of $\boldsymbol{E}$ and $\boldsymbol{H}$ with (8) and their Boltzmann equations (9), we use the suggested equilibria (10) from Ref. [23]. In order to obtain the Maxwell equations via (A9), we use a set of streaming vectors $\boldsymbol{v}_i$ as shown in Fig. 1 that fulfill the needed relations in form of

$$\sum_{i=1}^{6}v_{\alpha,i}=0, \tag{B1a}$$

$$\sum_{i=1}^{6}v_{\alpha,i}v_{\beta,i}=6\delta_{\alpha\beta}. \tag{B1b}$$

Following Appendix A, we obtain for (A9) by replacing f_i with $e_{\alpha,i}$ and f_i^{eq} with (10a) and the usage of (B1a) approximately

$$\begin{aligned} 0&=\sum_{i=1}^{6}\frac{1}{6}(\partial_t+\sum_\eta v_{\eta,i}\partial_\eta)\left(\varepsilon_r E_\alpha-\sum_{\beta,\gamma}\epsilon_{\alpha\beta\gamma}v_{\beta,i}H_\gamma\right)\\ &=\sum_{i=1}^{6}\frac{1}{6}\Big[\varepsilon_r\partial_t E_\alpha-\sum_{\beta,\gamma}\epsilon_{\alpha\beta\gamma}v_{\beta,i}\partial_t H_\gamma\\ &\quad+\sum_\eta\left(\varepsilon_r v_{\eta,i}\partial_\eta E_\alpha-\sum_{\beta,\gamma}\epsilon_{\alpha\beta\gamma}v_{\beta,i}v_{\eta,i}\partial_\eta H_\gamma\right)\Big]\\ &\equiv\sum_{i=1}^{6}\frac{1}{6}\left(\varepsilon_r\partial_t E_\alpha-\sum_{\beta,\gamma,\eta}\epsilon_{\alpha\beta\gamma}v_{\beta,i}^2\delta_{\beta\eta}\partial_\eta H_\gamma\right). \end{aligned} \tag{B2}$$

Using (B1b) for (B2) and summing up over all i, we obtain (11a) in the form

$$0=\varepsilon_r\partial_t E_\alpha-\sum_{\beta,\gamma}\epsilon_{\alpha\beta\gamma}\partial_\beta H_\gamma. \tag{B3}$$

To obtain (11b), we repeat the procedure for (B2) and (B3) by replacing f_i with $h_{\alpha,i}$ and f_i^{eq} with (10b) and then obtain

$$\begin{aligned} 0&=\sum_{i=1}^{6}\frac{1}{6}(\partial_t+\sum_\eta v_{\eta,i}\partial_\eta)\left(\mu_r H_\alpha+\sum_{\beta,\gamma}\epsilon_{\alpha\beta\gamma}v_{\beta,i}E_\gamma\right)\\ &=\sum_{i=1}^{6}\frac{1}{6}\Big[\mu_r\partial_t H_\alpha+\sum_{\beta,\gamma}\epsilon_{\alpha\beta\gamma}v_{\beta,i}\partial_t E_\gamma\\ &\quad+\sum_\eta\left(\mu_r v_{\eta,i}\partial_\eta H_\alpha+\sum_{\beta,\gamma}\epsilon_{\alpha\beta\gamma}v_{\beta,i}v_{\eta,i}\partial_\eta E_\gamma\right)\Big]\\ &=\mu_r\partial_t H_\alpha+\sum_{\beta,\gamma}\epsilon_{\alpha\beta\gamma}\partial_\beta E_\gamma. \end{aligned} \tag{B4}$$

APPENDIX C: SEPARATED MODEL

The separation is an extension of the unseparated model derived in Appendix B in the limit of vacuum. Here all nonzero vectors $\boldsymbol{v}_i$ shown in Fig. 1 have been used. This extension now uses the zero vector that is assigned to the additional

distributions $e_{\alpha,0}$ and $h_{\alpha,0}$. These quantities hold the influence of polarization

$$P_\alpha := (\varepsilon_r - 1)E_\alpha \equiv e^{\mathrm{eq}}_{\alpha,0} \tag{C1}$$

and magnetization

$$M_\alpha := (\mu_r - 1)H_\alpha \equiv h^{\mathrm{eq}}_{\alpha,0} \tag{C2}$$

caused by the interaction of EM fields with media. The additional Boltzmann equations then read

$$\begin{aligned} e_{\alpha,0}(\boldsymbol{r},t+\delta t) &= 2e^{\mathrm{eq}}_{\alpha,0}(\boldsymbol{r},t) - e_{\alpha,0}(\boldsymbol{r},t), \\ h_{\alpha,0}(\boldsymbol{r},t+\delta t) &= 2h^{\mathrm{eq}}_{\alpha,0}(\boldsymbol{r},t) - h_{\alpha,0}(\boldsymbol{r},t) \end{aligned} \tag{C3}$$

and obey, following the derivation in Appendix A,

$$\begin{aligned} 0 &= \sum_{i=1}^{6}\left(\partial_t + \sum_\eta v_{\eta,i}\partial_\eta\right)[(\varepsilon_r - 1)E_\alpha] = (\varepsilon_r - 1)\partial_t E_\alpha, \\ 0 &= \sum_{i=1}^{6}\left(\partial_t + \sum_\eta v_{\eta,i}\partial_\eta\right)[(\mu_r - 1)E_\alpha] = (\mu_r - 1)\partial_t H_\alpha. \end{aligned} \tag{C4}$$

Referring now to Appendix B in the limit of vacuum ($\varepsilon_r := 1$ and $\mu_r := 1$ for $i \in [1,6]$), we add (C1) to (8a) that then reads

$$\varepsilon_r E_\alpha = \left[\sum_{i=1}^{6} e_{\alpha,i}\right] + e_{\alpha,0}. \tag{C5}$$

Accordingly to (B2), we obtain for (C5) the differential equation

$$\begin{aligned} 0 &= \left[\partial_t E_\alpha - \sum_{\beta,\gamma}\epsilon_{\alpha\beta\gamma}\partial_\beta H_\gamma\right] + (\varepsilon_r - 1)\partial_t E_\alpha \\ &= \varepsilon_r \partial_t E_\alpha - \sum_{\beta,\gamma}\epsilon_{\alpha\beta\gamma}\partial_\beta H_\gamma. \end{aligned} \tag{C6}$$

Analogously for H_α, we add (C2) to (8a) and obtain

$$\mu_r H_\alpha = \left[\sum_{i=1}^{6} h_{\alpha,i}\right] + h_{\alpha,0}, \tag{C7}$$

which leads by following (B4) to

$$\begin{aligned} 0 &= \left[\partial_t H_\alpha + \sum_{\beta,\gamma}\epsilon_{\alpha\beta\gamma}\partial_\eta E_\gamma\right] + (\mu_r - 1)\partial_t H_\alpha \\ &= \mu_r \partial_t H_\alpha + \sum_{\beta,\gamma}\epsilon_{\alpha\beta\gamma}\partial_\beta E_\gamma. \end{aligned} \tag{C8}$$

Both Eqs. (C6) and (C8) equal the propagating part of the Maxwell equations in (11). Note that ε_r and μ_r here are assumed to be constant.

[1] X. He and L.-S. Luo, Phys. Rev. E **56**, 6811 (1997).
[2] K. S. Kunz and R. J. Luebbers, *The Finite Difference Time Domain Method for Electromagnetics* (Taylor & Francis, Philadelphia, 1993).
[3] E. M. Salomons, W. J. A. Lohman, and H. Zhou, PLoS ONE **11**, e0147206 (2016).
[4] D. B. Dhuri, S. M. Hanasoge, P. Perlekar, and J. O. A. Robertsson, Phys. Rev. E **95**, 043306 (2017).
[5] D. Conrad, A. Schneider, and M. Böhle, J. Comput. Phys. **301**, 218 (2015).
[6] A. Yagub, H. Farhat, S. Kondaraju, and T. Singh, J. Comput. Phys. **301**, 402 (2015).
[7] A. Caiazzo and M. Junk, Comput. Math. Appl. **55**, 1415 (2008).
[8] D. Anderl, S. Bogner, C. Rauh, U. Rüde, and A. Delgado, Comput. Math. Appl. **67**, 331 (2014).
[9] S. Galindo-Torres, A. Scheuermann, L. Li, D. Pedroso, and D. Williams, Comput. Phys. Commun. **184**, 1086 (2013).
[10] M. Madadi and M. Sahimi, Phys. Rev. E **67**, 026309 (2003).
[11] J. Bao and L. Schaefer, Appl. Math. Model. **37**, 1860 (2013).
[12] R. Nourgaliev, T. Dinh, and B. Sehgal, Nucl. Eng. Des. **211**, 153 (2002).
[13] Z. Li, M. Yang, and Y. Zhang, Int. J. Heat Mass Transf. **70**, 864 (2014).
[14] W. Zhou, Y. Yan, and J. Xu, Intl. Commun. Heat Mass Transf. **55**, 113 (2014).
[15] Y. Guangwu, Acta Mech. Sinica **14**, 186 (1998).
[16] Y. Guangwu, J. Comput. Phys. **161**, 61 (2000).
[17] B. Shi and Z. Guo, Comput. Math. Appl. **61**, 3443 (2011).
[18] S. Succi and R. Benzi, Physica D **69**, 327 (1993).
[19] D. Lapitski and P. J. Dellar, Philos. Trans. R. Soc. London A **369**, 2155 (2011).
[20] P. J. Dellar, EPL (Europhy. Lett.) **90**, 50002 (2010).
[21] P. J. Dellar, J. Stat. Phys. **121**, 105 (2005).
[22] M. Mendoza and J. D. Muñoz, Phys. Rev. E **82**, 056708 (2010).
[23] Y. Liu and G. Yan, Appl. Math. Model. **38**, 1710 (2014).
[24] S. M. Hanasoge, S. Succi, and S. A. Orszag, EPL (Europhys. Lett.) **96**, 14002 (2011).
[25] R. Nourgaliev, T. Dinh, T. Theofanous, and D. Joseph, Int. J. Multiphase Flow **29**, 117 (2003).
[26] T. Lee and C.-L. Lin, J. Comput. Phys. **206**, 16 (2005).
[27] G. R. McNamara and G. Zanetti, Phys. Rev. Lett. **61**, 2332 (1988).
[28] A. A. Mohamad, *Lattice Boltzmann Method* (Springer, London, 2011).
[29] J. Meng and Y. Zhang, J. Comput. Phys. **230**, 835 (2011).
[30] A. A. Mohamad and A. Kuzmin, Int. J. Heat Mass Transf. **53**, 990 (2010).
[31] G. Strang, SIAM J. Num. Anal **5**, 506 (1968).
[32] B. Servan-Camas and F. T.-C. Tsai, Adv. Water Resour. **31**, 1113 (2008).
[33] A. N. Gorban and D. J. Packwood, Physica A **414**, 285 (2014).
[34] W. Hayt, *Engineering Electromagnetics*, 4th ed. (McGraw-Hill, New York, 1981).
[35] J. D. Sterling and S. Chen, J. Comput. Phys. **123**, 196 (1996).

[36] M. Rheinländer, Comput. Math. Appl. **59**, 2150 (2010).
[37] A. Bardow, I. V. Karlin, and A. A. Gusev, Phys. Rev. E **77**, 025701 (2008).
[38] R. Ostilla-Monico, Y. Yang, E. van der Poel, D. Lohse, and R. Verzicco, J. Comput. Phys. **301**, 308 (2015).
[39] Z. Guo, C. Zheng, and T. S. Zhao, J. Sci. Comput. **16**, 569 (2001).
[40] K. Sankaranarayanan, I. G. Kevrekidis, and S. Sundaresan, J. Fluid Mech. **452**, 61 (2002).
[41] R. A. Brownlee, A. N. Gorban, and J. Levesley, Phys. Rev. E **74**, 037703 (2006).
[42] R. A. Brownlee, A. N. Gorban, and J. Levesley, Phys. Rev. E **75**, 036711 (2007).
[43] B. Shi and Z. Guo, Phys. Rev. E **79**, 016701 (2009).